Chemical interaction at the $MoO_3/CH_3NH_3PbI_{3-x}Cl_x$ interface

Xiaxia Liao[1,2,], Severin N. Habisreutinger[3], Sven Wiesner[4], Golnaz Sadoughi[3], Daniel Abou-Ras[5], Marc A. Gluba[6], Regan G. Wilks[2,7], Roberto Félix[2], Marin Rusu[5], Robin J. Nicholas[3], Henry J. Snaith[3], and Marcus Bär[2,7,8,9*]*

[1]School of Materials Science and Engineering, Nanchang University, Nanchang 330031, P.R. China

[2]Department Interface Design, Helmholtz-Zentrum Berlin für Materialien und Energie GmbH (HZB), Albert-Einstein-Str. 15, 12489 Berlin, Germany

[3]Department of Physics, Clarendon Laboratory, University of Oxford, Oxford, OX1 3PU, UK

[4]Institute Functional Oxides for Energy-Efficient IT, HZB, Hahn-Meitner-Platz 1, 14109 Berlin, Germany

[5]Structure and Dynamics of Energy Materials, HZB, Hahn-Meitner-Platz 1, 14109 Berlin, Germany

[6]Institute for Silicon Photovoltaics, HZB, Kekulestr. 5, 12489 Berlin, Germany

[7]Energy Materials In-situ Laboratory Berlin (EMIL), HZB, Albert-Einstein-Str. 15, 12489 Berlin, Germany

[8]Helmholtz-Institute Erlangen-Nürnberg for Renewable Energy (HI ERN), Albert-Einstein-Str. 15, 12489 Berlin, Germany

[9]Department of Chemistry and Pharmacy, Friedrich-Alexander-Universität Erlangen-Nürnberg (FAU), Egerlandstr. 3, 91058 Erlangen, Germany

*corresponding authors: liaoxiaxia@ncu.edu.cn; marcus.baer@helmholtz-berlin.de

Keywords: MoO_3, halide perovskite solar cell, interface, hard x-ray photoelectron spectroscopy, decomposition

ABSTRACT

The limited long-term stability of metal halide perovskite – based solar cells is a bottleneck in their drive toward widespread commercial adaptation. The organic hole transport materials (HTMs) have been implicated in the degradation, and metal oxide layers are proposed to as alternatives. One of the most prominent metal oxide HTM in organic photovoltaics is MoO_3. However, the use of MoO_3 as HTM in metal halide perovskite – based devices causes a severe solar cell deterioration. Thus, the formation of the $MoO_3/CH_3NH_3PbI_{3-x}Cl_x$ ($MAPbI_{3-x}Cl_x$) heterojunction is systematically studied by synchrotron-based hard x-ray photoelectron spectroscopy, scanning electron microscopy, energy-dispersive x-ray spectroscopy, and Raman spectroscopy. Upon MoO_3 deposition, significant chemical interaction is induced at the $MoO_3/MAPbI_{3-x}Cl_x$ interface: Substoichiometric molybdenum oxide is present, and the perovskite decomposes in the proximity of the interface, leading to accumulation of PbI_2 on the MoO_3 cover layer. Furthermore, we find evidence for the formation of new compounds such as $PbMoO_4$, PbN_2O_2, and PbO as a result of the $MAPbI_{3-x}Cl_x$ decomposition and suggest chemical reaction pathways to describe the underlying mechanism. These findings suggest that the (direct) $MoO_3/MAPbI_{3-x}Cl_x$ interface may be inherently unstable. It provides an explanation for the low power conversion efficiencies of metal halide perovskite solar cells that use MoO_3 as hole-transport material and in which there is a direct contact between MoO_3 and perovskite.

KEYWORDS: Molybdenum oxide, Halide perovskite, Interface properties, hard X-ray photoelectron spectroscopy,

INTRODUCTION

Recent advances in organic-inorganic hybrid perovskite photovoltaic devices may underpin a revolutionary step in the exploitation of solar energy. However, the stability of perovskite-based solar cells is one of the great challenges for the commercialization of this PV technology.[1-3] In addition to the degradation of the perovskite material under ambient conditions,[4] the standard hole-transport material (HTM) used in record efficiency devices, 2,2',7,7'-tetrakis(N,Ndi-p-methoxyphenyl-amine) 9,9-spirobifluorene (Spiro-OMeTAD), has additional issues (e.g., high cost and low conductivity).[5] Thus, efforts have been made to replace the Spiro-OMeTAD layer with other, more stable materials. In organic solar cells, the use of MoO_3 as an HTM can considerably enhance the stability of the device;[6-7] it has therefore also been employed in perovskite-based solar cells in an attempt to achieve similar results.[8] The power conversion efficiencies of such devices (where MoO_3 is in direct contact with the perovskite) are, however, very low (i.e., < 1 %).[9] Only cells in which an "interlayer" (of, e.g., Spiro-OMeTAD) separates the MoO_3 and the perovskite show competitive efficiencies,[9]

indicating that either the chemical or the electronic structure of the MoO_3/perovskite interface is not suitable for high device performance. Some reports indeed indicate a chemical interaction at the MoO_3/perovskite interface.[10-12] Thibau et al.[13] and Li et al.[14] report that the insertion of a thin N,N'(1-dinaphthyl-N,N'diphenyl-(1,1'-biphenyl-4,4'-diamine)) (NPB) layer can largely prevent this process. However, the underlying chemical mechanism of the interfacial interaction and detailed insight into what species are formed upon deposition of MoO_3 on the perovskite remains largely unclear.

In our contribution, we thoroughly study the MoO_3/$MAPbI_{3-x}Cl_x$ interface by hard x-ray photoelectron spectroscopy (HAXPES). In addition, complementary Raman, energy-dispersive x-ray spectroscopy (EDX), and scanning electron microscopy (SEM) measurements were performed to gain laterally resolved and structural information. This combination of analysis methods gives detailed insights into the chemical interaction at the interface allowing the identification of decomposition products at a level not possible before; a crucial prerequisite for understanding the underlying causes of the limited performance of MoO_3/perovskite devices.

EXPERIMENTAL SECTION

Sample preparation

Device-relevant $MAPbI_{3-x}Cl_x$ perovskite thin films of 300 nm nominal thickness were prepared on compact TiO_2/SnO_2:F/glass substrates at University of Oxford following the standard "one-pot" preparation approach.[15] The prepared $MAPbI_{3-x}Cl_x$ precursor solution was spin-coated onto compact TiO_2 at 2000 rpm for 45 s inside a N_2 filled glovebox. After the spin-coating, the prepared films were left inside the glovebox at room temperature to allow the solvent to evaporate, followed by an annealing step (2.5 h at 90°C) for perovskite crystallization. After preparation, the samples were sealed under inert gas and transported to the HZB for MoO_3 deposition and characterization in a gastight container. At HZB, the samples were unpacked in a dry-N_2 glovebox directly attached to the MoO_3 deposition vacuum chamber. MoO_3 layers of 3 nm, 20 nm, and 50 nm thickness were prepared by physical vapor deposition on the $MAPbI_{3-x}Cl_x$/TiO_2/FTO/glass stack using a growth rate of approximately 0.5Å/s as described previously.[16-17] A PbI_2 powder sample (Sigma-Aldrich, 99.999% trace metals basis) was used as a reference for the HAXPES measurements; it was mounted onto the sample holder on a double-sided carbon tape.

Characterization

HAXPES measurements were conducted at the HiKE endstation[18] located at the KMC-1 bending magnet beamline[19] of HZB's synchrotron facility BESSY II. HiKE is equipped with a Scienta R4000 electron energy analyzer and operated in ultra-high vacuum (UHV) conditions: base pressure in the analysis chamber is $<10^{-8}$ mbar. Sample transport and mounting was performed under inert gas atmosphere. For the HAXPES measurements, the excitation energy was set to 2003 eV (henceforth simply called "2 keV"). The pass energy and energy step width were 200 eV and 0.1 eV, respectively, for all the core level measurements and 500 eV and 0.5 eV for the survey scans. The binding energy (BE) scale of the HAXPES spectra was calibrated using Au 4f reference measurements of a clean Au foil; the Au $4f_{7/2}$ core level line was set to 84.00 eV. The total energy resolution of the core level spectra was approximately 0.25 eV. The information depth of the measurement is determined by the exponential attenuation of the photoelectrons according to the kinetic energy-dependent inelastic mean free path (IMFP), which is approximately 3 nm for the shallow core levels excited by 2 keV in MoO_3.[20-21] The exponential attenuation of the photoemission signal means that 95% of the signal comes from within 3×IMFP of the surface, and 98% comes from within 4×IMFP of the surface. For a homogeneous capping layer on a substrate, this means that the absence of photoemission signals from the substrate indicates a capping layer thickness of >3-4×IMFP depending on the composition and therefore signal intensity of the substrate. Taking into account our previous findings on x-ray induced reduction of MoO_3 films, we optimized measurement parameters and limited exposure time to 1-2 h per probed sample spot to reduce artefacts due to beam damage.[16] For quantification and analysis of the HAXPES data, the same photoemission lines of the whole sample set were fit simultaneously using a linear background and Voigt profiles with linked widths and shapes. However, for the fit of the Mo 3d line a different (narrower) line profile was allowed for the 50 nm MoO_3/$MAPbI_{3-x}Cl_x$ sample compared to the samples with 3 and 20 nm MoO_3, as justified in the discussion of the Mo 3d related findings below. Doublets were used to fit the Pb 4f and Mo 3d spectra, with Voigt functions with intensity ratios of 4:3 and 3:2 (based on the 2j+1 multiplicity) representing the $4f_{7/2}$, $4f_{5/2}$ and $3d_{5/2}$, $3d_{3/2}$, respectively. The separation due to spin-orbit splitting, determined during the fit routine, was 4.86 eV for the Pb 4f and 3.15 eV for the Mo 3d.[22-24]

SEM images of the sample surface were taken with a LEO GEMINI 1530 from Zeiss by measuring secondary electrons at a working distance of 4.8 mm and an acceleration voltage of 3 kV for the primary electron beam. EDX elemental distribution maps were acquired using a Zeiss UltraPlus scanning electron microscope equipped with an Oxford Instruments X-Max 80 X-ray detector and the AZtec acquisition and evaluation software. The beam energy was 5 keV and the beam current approximately 1 nA. The information depth at this energy is in the micrometer range.

Raman spectra are acquired by a laser with a wavelength of 457.9 nm and a power of 1 mW. The information depth is around several hundred of nanometers.

For the SEM, EDX, and Raman (in contrast to the HAXPES) investigations, the samples were briefly exposed to ambient conditions prior measurement.

RESULTS & DISCUSSION

SEM and EDX show the MoO_3 layer formation on top of a metal halide perovskite film; a representative SEM image of the 50 nm MoO_3/$MAPbI_{3-x}Cl_x$ sample is presented in Figure 1(a) (top panel). Some areas in the image appear lighter than the rest of the sample. In the corresponding EDX maps, where we look at the L, K, and M atomic transitions, inhomogeneous elemental distributions on the surface of the sample are clearly shown. Note that SEM and EDX measurements on the bare $MAPbI_{3-x}Cl_x$ sample do not show these inhomogeneities (see Supporting Information, S.I., Figure S1). As can be seen in the Mo L and O K maps (Figure 1(d) and (e)), the areas that appear light in the SEM image are void of Mo and O. At the same time, an increased amount of Pb and I in these areas can be identified in the Pb M map (Figure 1(b)) and – despite the significantly lower signal-to-noise-ratio – in the I M map (Figure 1(c)), respectively. The C K map (Figure 1(f)) also indicates the depletion of C, while the N K map (Figure 1(g)), shows a more homogeneous N distribution, presumably due to insufficient signal-to-noise ratio. From this, we conclude that Pb and I accumulate in these sample regions (most likely in the form of PbI_2) that extend from the surface deep into the $MAPbI_{3-x}Cl_x$, suggesting decomposition of the $MAPbI_{3-x}Cl_x$ layer upon MoO_3 deposition. Similar results have been reported by Matteocci et al., they observed iodine diffusion in the top HTM layer in cross-sectional EDX maps.[25] This is corroborated by the fact that I^- has a lower activation energy than MA^+ or Pb^- for vacancy-mediated ion migration,[26] i.e., it has the highest diffusion coefficient.

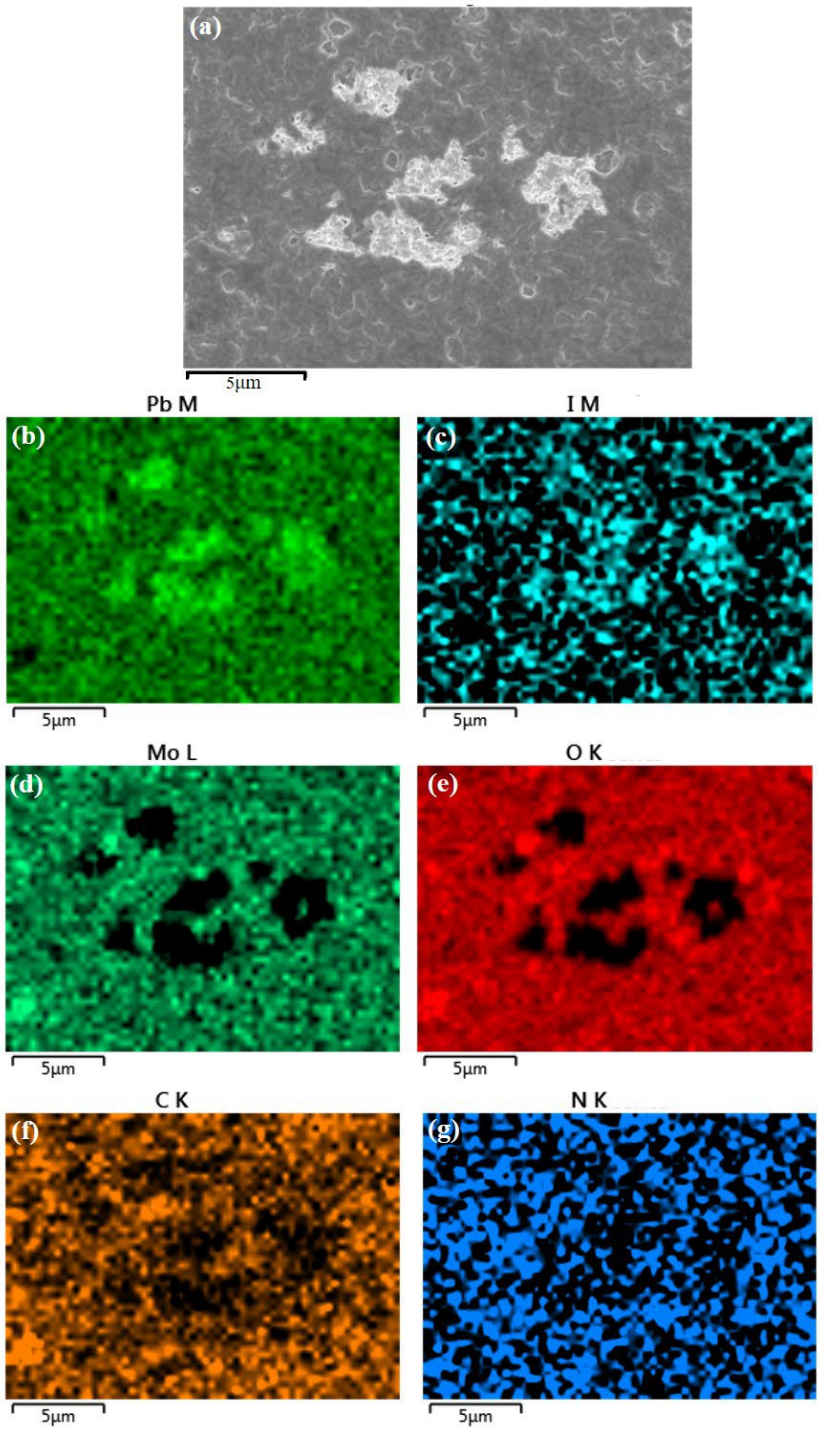

Figure 1 (a) SEM image of the 50 nm MoO_3/$MAPbI_{3-x}Cl_x$ sample and the related (b) Pb M, (c) I M, (d) Mo L, (e) O K, (f) C K, and (g) N K EDX maps of the same area.

In order to study the interface formation, a MoO_3 thickness series (with nominal thicknesses of 0 [i.e., uncovered/bare], 3, 20, and 50 nm) on $MAPbI_{3-x}Cl_x$/compact TiO_2/SnO_2:F/glass substrates were characterized by HAXPES. Figure S2 (see S.I.) displays the respective survey spectra. All expected core level lines are observed, most prominently the I 3d, (O 1s,) N 1s, C 1s, (Mo 3d,) and Pb 4f peaks.

For the uncovered (i.e., "bare") $MAPbI_{3-x}Cl_x$ sample, there are no Ti- (most prominent: Ti $2p_{3/2}$ at 454 eV BE) or Sn- (most prominent: Sn $3d_{5/2}$ at 485 eV BE) related core levels detected, indicating a complete coverage of the compact TiO_2/SnO_2:F/glass substrate by the perovskite. Also, no Cl signal (most prominent: Cl $2p_{3/2}$ at 200 eV BE) is observed, which can be explained since most of the Cl is expected to be lost during the film formation and crystalisation.[27-28] Upon MoO_3 deposition, O 1s and Mo 3d signals appear and increase with nominal thickness, as expected. The $MAPbI_{3-x}Cl_x$-related photoemission lines are attenuated with increasing MoO_3 thickness, however; they can clearly still be observed in the spectra of the samples that have (nominal) 20 and 50 nm MoO_3 cover layer thicknesses, to some extent in agreement with the SEM and EDX results discussed above.

To get detailed insight into the chemical interaction at the $MoO_3/MAPbI_{3-x}Cl_x$ interface, the HAXPES detail spectra are discussed next. The Pb 4f and Mo 3d spectra are shown in Figure 2a and 2b. Figures S3 and S4 (see S.I.) show the corresponding I 3d, N 1s (Mo 3p, Pb 4d), C 1s, and O 1s spectra including fit analysis. For the bare $MAPbI_{3-x}Cl_x$ sample, we find a Pb 4f spectrum that can be well described with one Voigt profile (Pb_I) at (138.37 ± 0.02) eV BE, which we ascribe to Pb in a perovskite environment. Note that the Pb 4f line is found at a very similar BE as in the corresponding spectrum of the PbI_2 powder reference (BE (PbI_2) = 138.48 ± 0.02 eV), suggesting that based on the Pb 4f data alone, it is not possible to differentiate between perovskite Pb or PbI_2 (in agreement with reports in literature, see S.I. Figure S5). The I 3d line is also insensitive to the differences between I in $MAPbI_{3-x}Cl_x$ or in PbI_2, see S.I. Figure S3(a). However, we do not find indications for the presence of significant amounts of metallic Pb (BE_{Pb4f}: 136.80-137.11eV[11, 23-24, 27]), which has been observed in previous studies.[24, 27] For the $MoO_3/MAPbI_{3-x}Cl_x$ samples we, however, find additional spectral intensity at higher BE (138.90 ± 0.02 eV), which increases with MoO_3 thickness and is attributed to (at least) one additional lead species (component Pb_{II}) that increases with nominal MoO_3 thickness. Below, we will attempt to identify the species in conjunction with complementary Raman measurements.

Focusing next on the MoO_3 layer, the Mo 3d detail spectra (Figure 2b) show the expected increase in intensity as a function of nominal layer thickness as well as a change in the spectral shape. Curve fits of the Mo 3d spectra show that the spectra of all samples need two spin-orbit split doublets (Mo_I and Mo_{II}), which we ascribe to Mo^{6+} (Mo_I: $BE_{Mo3d5/2}$ = 232.96 ± 0.02 eV) and Mo^{5+} (Mo_{II}: $BE_{Mo3d5/2}$ = 231.92 ± 0.02 eV).[12] The $Mo_{II}/Mo_I = Mo^{5+}/Mo^{6+}$ ratio decreases with increasing MoO_3 thickness, which we ascribe to the formation of an oxygen-deficient molybdenum oxide (MoO_x with $x<3$, see S.I. Figure S6) at the $MoO_x/MAPbI_{3-x}Cl_x$ interface, in agreement with previous reports. The reduced amount of MoO_x might lead to a decreased 'disorder' in the deposited material, which results in a reduced variation of bond angles and distances in the MoO_3 further away from the chemical

interaction at the interface, explaining the narrower line shape of the Mo 3d signal of the 50 nm $MoO_x/MAPbI_{3-x}Cl_x$ sample.

The N 1s line is in a similar BE region as the Pb $4d_{5/2}$ and the Mo 3p photoemission lines, see S.I. Figure S3 (b). One Voigt profile is sufficient to fit the N 1s contribution reasonably well, and we attribute it to nitrogen in a perovskite environment for the bare $MAPbI_{3-x}Cl_x$ sample and (to some extent) for the samples with a thin MoO_3 layer (in agreement with literature, see S.I., Figure S7). Below, based on complementary Raman measurements and the overall intensity evolution of the photoemission lines, we attempt to clarify the chemical structure of nitrogen for the samples with thick(er) MoO_3 layers., i.e., samples for which the presence of PbI_2 was already suggested. In contrast to the Pb_I component of the Pb 4f and the I 3d line, Figure S3(b) shows that the N 1s intensity does not decrease with (nominal) MoO_3 thickness, similar to the Pb_{II} Pb 4f component (see Figure 2(a)). Similarly to the Mo 3d, also the Mo 3p line has to be fitted with two contributions ascribed to Mo^{5+} and Mo^{6+} (see discussion in conjunction to Fig. 2(b)) above).

The C 1s detail spectra of the $MoO_3/MAPbI_{3-x}Cl_x$ sample series is shown in Figure S4(a). Two Voigt profiles (C_I and C_{II}) are required to fit the spectra reasonably well. The low BE contribution C_I is attributed to aliphatic and/or "adventitious" carbon, in agreement with literature reports (see S.I., Figure S8). C_{II} is – at least in the early stages of MoO_3 deposition – ascribed to C-N bonds from the MA cation (and thus it presents intact perovskite). After an initial increase of the C_I/C_{II} ratio upon the deposition of the thinnest (nominal 3 nm) MoO_3 layer due to an enhanced C_I content, the ratio decreases for thicker MoO_3 mainly by an increase of the C_{II} component (see Figure S4(a)). This finding could be explained by the formation of C-O bonds as a result of continued MoO_3 deposition and $MAPbI_{3-x}Cl_x$ decomposition. However, carbon-containing MA-related decomposition products like CH_3NH_2 (similar BE_{C1s} as C_{II}, see Figure S8) or CH_3I (similar BE_{C1s} as C_I, see Figure S8) that are produced when PbI_2 is formed[29-30] may also have an impact on the C_I/C_{II} ratio evolution.

The low-intensity O 1s line of the bare $MAPbI_{3-x}Cl_x$ sample (see S.I. Figure S4(b)), indicating that air-exposure during sample transfer was successfully minimized, can be fitted with one (broad) Voigt profile O_I at BE = (532.50 ± 0.02) eV, which we ascribe to hydroxide – like surface contaminants. Upon MoO_3 deposition, the O 1s spectrum shifts to lower BE and changes its shape. The O 1s spectra of all three $MoO_3/MAPbI_{3-x}Cl_x$ samples can be fit with a low-intensity (broad) contribution O_{II} at BE_{O1s} = (531.90 ± 0.02) eV and a high-intensity Voigt profile O_{III} at BE_{O1s} = (530.70 ± 0.02) eV. In agreement with literature (see S.I. Figure S9), we (partially) attribute the dominant peak (O_{III}) to oxygen in molybdenum (sub)oxide. The identification of the smaller O_{II} and O_I peaks is not as

straightforward. The report from Godding et al. attributed these two high BE peaks to hydroxide and organic C=O group-related surface contaminants.[31]

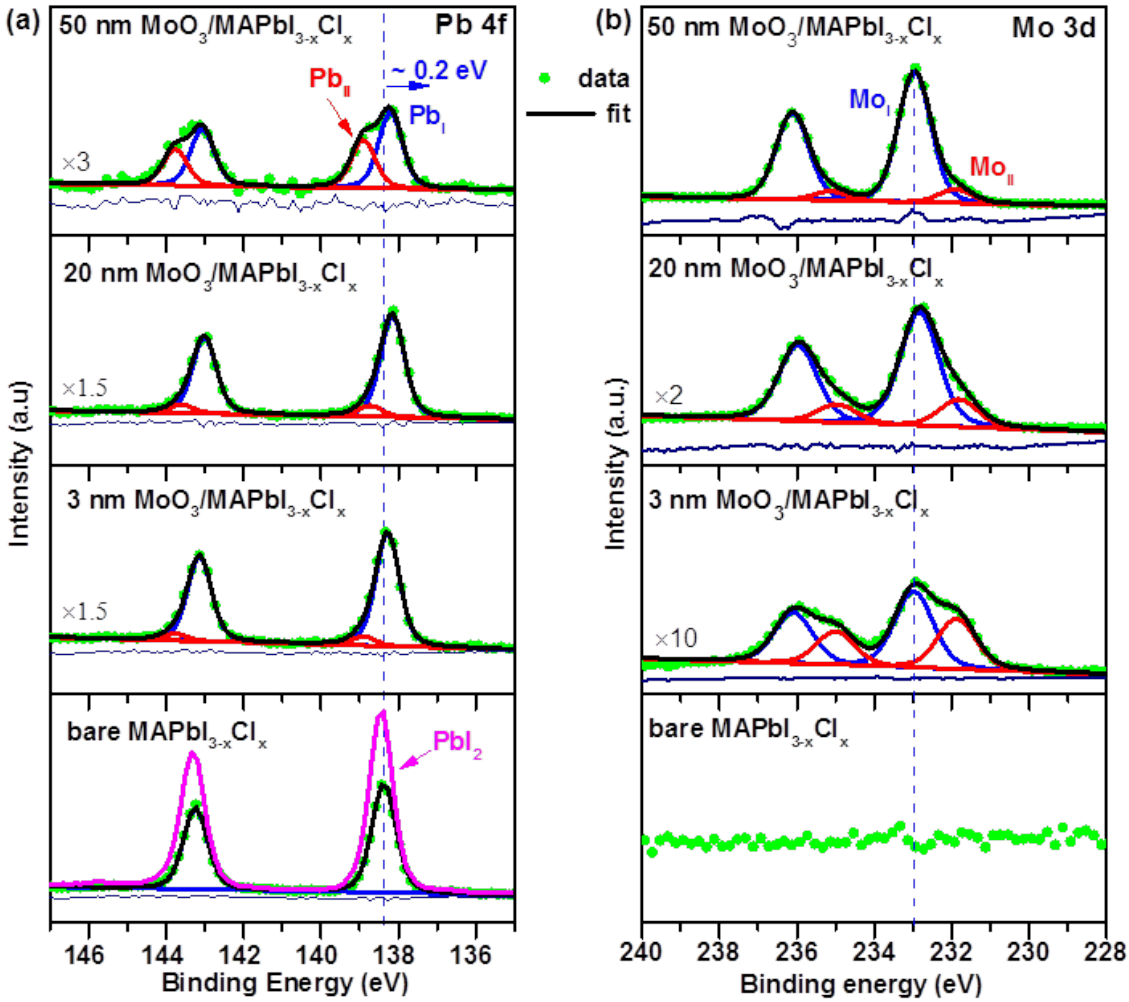

Figure 2 2 keV excited HAXPES Pb 4f (a) and Mo 3d (b) detail spectra of the $MAPbI_{3-x}Cl_x$ sample before ("bare") and after deposition of MoO_3 layers of 3, 20, and 50 nm nominal thickness. For comparison, the Pb 4f spectrum of the PbI_2 reference is shown directly on top of the respective spectrum of the bare $MAPbI_{3-x}Cl_x$ sample. The raw data is shown as green dots, the fit components as red and blue solid lines, and the total fit as a black solid line. To show the photoemission lines on similar intensity levels, different magnification factors were applied (indicated as e.g., "×10" where appropriate). The respective residua (i.e., the difference between the raw data and the fit) are shown below each spectrum.

Raman measurements were performed to identify the chemical species formed upon deposition of MoO_3 on $MAPbI_{3-x}Cl_x$. As shown in Figure 3, the bare $MAPbI_{3-x}Cl_x$ sample exhibits a strong band at 145 cm^{-1} ascribed to the motion of MA^+ in the perovskite cage and a weak MA^+ torsional mode at 287 cm^{-1}.[32] Upon deposition of 50 nm MoO_3, these Raman modes are greatly reduced and the peak at 110 cm^{-1} is enhanced. Despite the distorting impact of the laser excitation absorption edge, we

tentatively ascribe (some of) this feature to the Pb-I stretching mode of PbI_2,[33-34] corroborating our suggestion above that lead iodide is formed upon MoO_3 deposition. Furthermore, new peaks can be observed; most prominently at 519, 872, and 1600 cm^{-1}. These vibrations are attributed to a metal (lead) hyponitrite ($-N_2O_2$) species (515 cm^{-1}),[35] $PbMoO_4$ (870 cm^{-1}),[36] and 'disordered' carbon (1500-1700 cm^{-1}),[37] respectively, further corroborating the decomposition of $MAPbI_{3-x}Cl_x$ upon MoO_3 deposition. Close inspection of the Raman spectrum of the 50 nm $MoO_3/MAPbI_{3-x}Cl_x$ sample (on a magnified scale, see insets in Figure 3) allows to identify more (minor) vibration signals, which affirm these attributions (see also Table S1 for reference - note that the stated positions of the $-N_2O_2$ vibrations are based on IR data). The three vibration lines below 300 cm^{-1} (see inset in Figure 3) additionally suggest the formation of PbO, and even the presence of $PbCO_3$ (explaining the signal at 1045 cm^{-1}), cannot be excluded (see Table S1).

The formation/presence of these species at the $MoO_3/MAPbI_{3-x}Cl_x$ interface is in agreement with the HAXPES data discussed above. The corresponding Pb 4f, Mo 3d, N 1s, and O 1s BE positions for respective references found in literature (see S.I. Figures S5 – S7, S9) agree with the BE positions of the Pb_I Pb 4f component for PbO, the Pb_{II} Pb 4f component for $PbMoO_4$ and PbN_2O_2, the Mo_I Mo 3d component for $PbMoO_4$, the N 1s line for $-N_2O_2$, the O_{II} O 1s component for $-N_2O_2$, and the O_{III} O 1s component for $PbMoO_4$ and PbO.

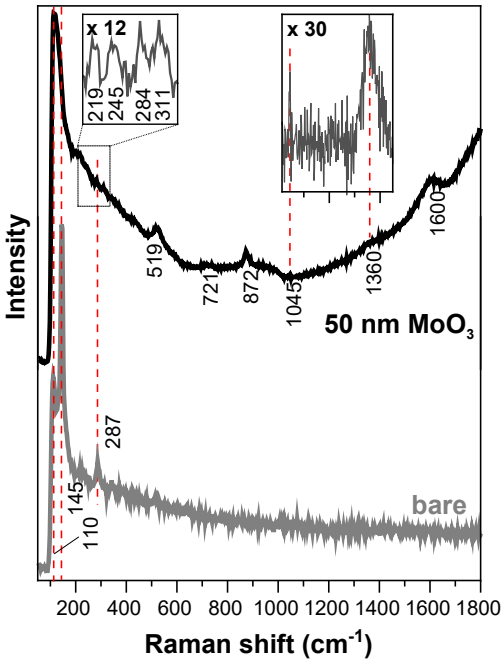

Figure 3 Raman spectra of bare perovskite ("bare") and the 50 nm $MoO_3/MAPbI_{3-x}Cl_x$ ("50 nm MoO_3") sample. The insets show the magnified view (× 12 or × 30, respectively) of the 50 nm $MoO_3/MAPbI_{3-x}Cl_x$ Raman spectrum from which a polynomial background has been subtracted.

The formation of PbI_2 is also in agreement with the Raman-derived photoluminescence (PL) signal (see S.I. Figure S10). After deposition of 50 nm MoO_3, a broad PL peak appears at 2440 cm^{-1} (0.3 eV). Considering the excitation energy of the 457.9 nm laser (2.7 eV), this corresponds to a PL signal centred around 2.4 eV, which is in excellent agreement with the optical band gap energy of PbI_2.[32] The band gap energies of other species that are suggested to form at the MoO_3/$MAPbI_{3-x}Cl_x$ interface are expected to be in this region.[38, 39]

To study the interface formation, we use the intensity of the most prominent $MAPbI_{3-x}Cl_x$- and MoO_3-related photoemission lines. The intensity evolution of the Pb 4f, I 3d, N 1s, C 1s, Mo 3d, and O 1s lines as derived from the survey spectra in Figure S2 is shown in Figure 4(a). The $MAPbI_{3-x}Cl_x$-related photoemission lines (except C 1s) attenuate with MoO_3 deposition, but the decreases occur at different rates, in the following order: I 3d, Pb 4f, N 1s (with N 1s showing the least attenuation). Some of the variation in intensity attenuation observed for the I 3d and Pb 4f lines can be explained by the lower binding (and thus higher kinetic) energy of the Pb 4f photoelectrons compared to that of the I 3d photoelectrons, resulting in a 25% higher IMFP. The remaining intensity deviation is attributed to the MoO_3 deposition-induced formation of (among others) PbI_2 (and its accumulation at the sample surface), which contains a higher relative amount of Pb compared to $MAPbI_{3-x}Cl_x$, and/or the formation of additional (I-free) Pb-species. The only slight decrease of the N 1s line and the increase of the C 1s line with (nominal) MoO_3 thickness suggests a complete decomposition of the perovskite in the proximity of the interface and the formation of other N- and C-containing species (e.g., PbN_2O_2 and/or MA-related decomposition products, see discussion above) that are then incorporated into the thicker growing (nominal) MoO_3 layer; the latter being in agreement with the increase of the Mo 3d and O 1s line intensities.

The intensity evolution of the spectra, further broken down into the individual fit components (from Figure 2, Figure S3 and S4), is shown in Figure 4(b). The I 3d line, which is attributed to $MAPbI_{3-x}Cl_x$ and PbI_2, decreases in a similar way as the Mo_{II} component of Mo 3d (attributed to Mo^{5+} (e.g., $MoO_{2.5}$)), and the O_I and O_{II} components of the O 1s line (attributed to O-H bonds). This suggests that PbI_2 and molybdenum suboxide are formed during the initial MoO_3 deposition process close to the interface and are then (together with the O-H bonds presumably formed at the bare perovskite) increasingly covered with the deposited (nominal) MoO_3 material, which attenuates their respective photoemission signals. With the Pb_I component of the Pb 4f line attributed to $MAPbI_{3-x}Cl_x$ or PbI_2, the intensity evolution of this component would be expected to follow a very similar trend as observed for the I 3d line. The observed discrepancy can be resolved if an additional (I-free) Pb species is formed during the MoO_3 deposition process, resulting in a Pb 4f contribution at a similar BE position as the one coming from $MAPbI_{3-x}Cl_x$ or PbI_2. The Raman data suggest that PbO is present, and the

Pb 4f line of PbO references is reported to be (within the reported energy variation) in a similar BE range as those of $MAPbI_{3-x}Cl_x$ or PbI_2 (see S.I., Figure S5). The Pb 4f spectra in Figure 2a show a slight shift to low BE upon MoO_3 deposition, also in agreement with suggested formation/presence of PbO. The Pb_{II} component of the Pb 4f line – ascribed to $PbMoO_4$ and/or PbN_2O_2 –increases with (nominal) MoO_3 thickness. The speciation is in agreement with the intensity evolution of the Mo_I component of the Mo 3d line, the O_{III} component of the O 1s line, and the N 1s line, respectively. These Pb species cannot be considered interface compounds in the classical sense (at least on this thickness scale) as their amounts seem to be proportional to the amount of (nominal) MoO_3 material deposited and thus increase instead of reaching highest concentration once the interface region is fully formed. So one might speculate that $PbMoO_4$ and/or PbN_2O_2 migrate towards the surface during MoO_3 deposition. The variation in the C_I and C_{II} component of the C 1s line indicates a complicated situation for carbon as a result of the MA decomposition and (most likely partial) incorporation into the deposited material.

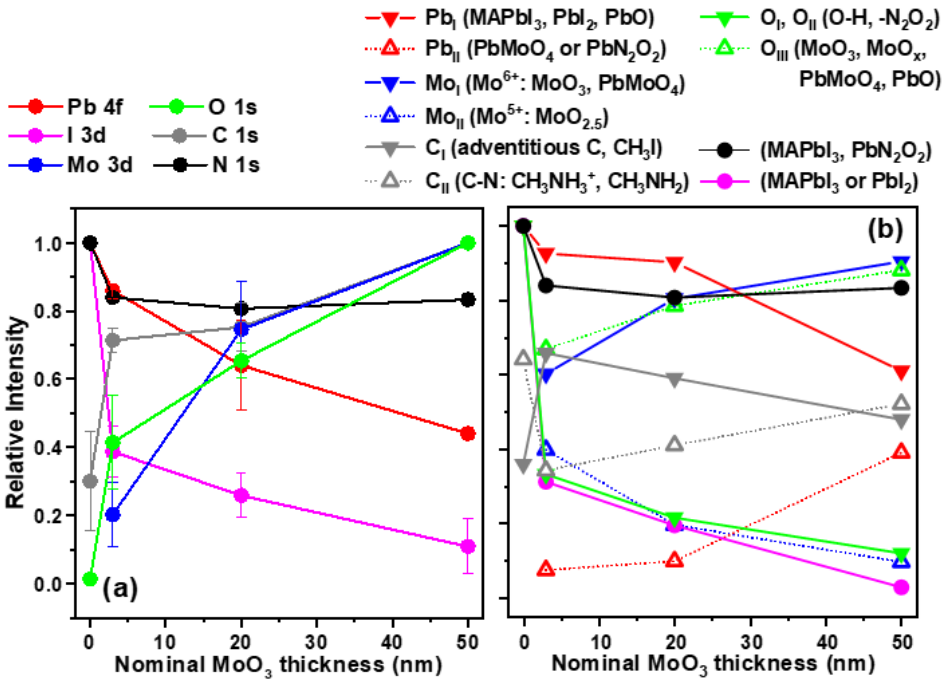

Figure 4 (a) Relative intensity evolution of Pb 4f, I 3d, C 1s, N 1s and Mo 3d, O 1s lines as a function of (nominal) MoO_3 thickness. The Pb 4f, I 3d, N 1s (Mo 3d, O 1s, C 1s) line intensities are depicted normalized to 1 for the bare $MAPbI_{3-x}Cl_x$ (the 50 nm $MoO_3/MAPbI_{3-x}Cl_x$) sample. (b) Relative intensity evolution of the line components and their attribution to different chemical species as a function of (nominal) MoO_3 thickness.

Based on the above discussion, we propose chemical reactions that may take place upon the deposition of MoO_3 on $MAPbI_{3-x}Cl_x$ interface (for simplicity and since no Cl is detected at the perovskite surface – we use $MAPbI_3$ in the following) and that may explain the formation of the suggested decomposition products PbI_2, $PbMoO_4$, PbN_2O_2, PbO, and $MoO_{2.5}$:

(1) $2CH_3NH_3PbI_{3\,(s)} + 3MoO_{3\,(s)} \rightarrow 2CH_3NH_3I_{\,(s)} + PbMoO_{4\,(s)} + PbI_{2\,(s)} + 2MoO_{2.5\,(s)} + I_{2\,(g)}$

(2) $2CH_3NH_3I_{\,(s)} + PbI_{2\,(s)} + 2O_{2\,(g)} \rightarrow PbN_2O_{2\,(s)} + 2H_2O_{\,(l)} + CH_3I_{\,(g)} + 2\,HI_{\,(g)}$

(3) $PbI_{2\,(s)} + 2H_2O_{\,(l)} \rightarrow PbO_{\,(s)} + 2\,HI_{\,(g)}$

Initially, the deposition of MoO_3 directly on $MAPbI_3$ may induce perovskite decomposition and formation of PbI_2, $PbMoO_4$, and $MoO_{2.5}$. In a second step, CH_3NH_3I may further decompose, forming together with the PbI_2 from reaction 1 and oxygen (present as a result of the formation of molybdenum suboxides and/or being present in the deposition chamber as a result of the sputter process of MoO_3) to PbN_2O_2. In reaction 3, the water formed in reaction 2 together with the PbI_2 formed in reaction 1 may react to form PbO. Note that the gaseous decomposition products may be readily pumped away due to the high vacuum in the deposition chamber and thus might not be efficiently incorporated into the cover layer.

CONCLUSION

In this contribution, we have investigated the formation of the $MoO_3/MAPbI_{3-x}Cl_x$ interface by hard x-ray photoelectron spectroscopy and Raman spectroscopy. Significant interfacial interactions are observed, and both materials are unstable when in direct contact with each other. Besides the formation of substoichiometric molybdenum oxide ($MoO_{2.5}$) and the accumulation of PbI_2 on the (nominal) MoO_3 surface, we find evidence for the presence of $PbMoO_4$, PbN_2O_2, and PbO. The formation of these species can easily be explained by a decomposition of the $MAPbI_{3-x}Cl_x$ material upon MoO_3 deposition, and corresponding chemical reactions pathways are suggested. Our finding clearly explains why the direct MoO_3/perovskite interface is not suitable to achieve high device performance. To prevent the detrimental chemical interaction at the $MoO_3/MAPbI_{3-x}Cl_x$ interface and allow lossless charge carrier transport, a suitable (chemically inert) interlayer that retains effective hole transfer is required. Potential candidates are NPB – based interlayers[13,14] or even other metal oxides (such as Al_2O_3) if deposited with a soft deposition route (e.g., atomic layer deposition).[40]

ASSOCIATED CONTENT

Supporting Information

The Supporting Information is available free of charge at ….

Complementary SEM/EDX images of the bare $MAPbI_{3-x}Cl_x$ sample, HAXPES survey spectra of the bare $MAPbI_{3-x}Cl_x$ sample and MoO_3(3 nm, 20 nm, 50 nm)/ $MAPbI_{3-x}Cl_x$ samples; fit of the I 3d, N 1s/Mo 3p/Pb 4d, C 1s, and O 1s detail HAXPES spectra; reference binding energy distributions of Pb $4f_{7/2}$, Mo $3d_{5/2}$, N 1s, C 1s, and O 1s for relevant compounds; Raman modes observed for the 50 nm $MoO_3/MAPbI_{3-x}Cl_x$ sample compared to that of relevant compounds, PL spectra of the bare $MAPbI_{3-x}Cl_x$ and 50 nm $MoO_3/MAPbI_{3-x}Cl_x$ samples.

AUTHOR INFORMATION

Corresponding Author

E-mail: liaoxiaxia@ncu.edu.cn, marcus.baer@helmholtz-berlin.de.

Acknowledgements

XL, RGW, RF, and MB acknowledge financial support by the Impuls- und Vernetzungsfonds of the Helmholtz-Association (VH-NG-423). Furthermore, XL is grateful to the Robert Bosch Stiftung for receiving funding through the Sustainable Partners – Partners for Sustainability program (32.05.8003.0112.0) and National Natural Science Foundation of China (No. 11804142). SNH, GS, RJN and HJS received support from the Engineering and Physical Science Research Council, UK. Finally, we thank HZB for the allocation of synchrotron radiation beamtime.

REFERENCES

1. Ou, Q.-D.; Li, C.; Wang, Q.-K.; Li, Y.-Q.; Tang, J.-X., Recent Advances in Energetics of Metal Halide Perovskite Interfaces. *Advanced Materials Interfaces* **2017**, *4*, 1600694.

2. Williams, S. T.; Rajagopal, A.; Chueh, C.-C.; Jen, A. K. Y., Current Challenges and Prospective Research for Upscaling Hybrid Perovskite Photovoltaics. *The Journal of Physical Chemistry Letters* **2016**, *7*, 811-819.

3. Green, M. A.; Ho-Baillie, A.; Snaith, H. J., The Emergence of Perovskite Solar Cells. *Nature Photonics* **2014**, *8*, 506-514.

4. Rong, Y.; Liu, L.; Mei, A.; Li, X.; Han, H., Beyond Efficiency: The Challenge of Stability in Mesoscopic Perovskite Solar Cells. *Advanced Energy Materials* **2015**, *5*, 1501066.

5. Sfyri, G.; Kumar, C. V.; Sabapathi, G.; Giribabu, L.; Andrikopoulos, K. S.; Stathatos, E.; Lianos, P., Subphthalocyanine as Hole Transporting Material for Perovskite Solar Cells. *RSC Advances* **2015**, *5*, 69813-69818.

6. Hu, X.; Chen, L.; Chen, Y., Universal and Versatile MoO_3-Based Hole Transport Layers for Efficient and Stable Polymer Solar Cells. *The Journal of Physical Chemistry C* **2014**, *118*, 9930-9938.

7. Gong, Y. S.; Dong, Y. M.; Zhao, B.; Yu, R. N.; Hu, S. Q.; Tan, Z. A., Diverse Applications of MoO_3 for High Performance Organic Photovoltaics: Fundamentals, Processes and Optimization Strategies. *Journal of Materials Chemistry A* **2020**, *8*, 978-1009.

8. Pérez-del-Rey, D.; Gil-Escrig, L.; Zanoni, K. P. S.; Dreessen, C.; Sessolo, M.; Boix, P. P.; Bolink, H. J., Molecular Passivation of MoO_3: Band Alignment and Protection of Charge Transport Layers in Vacuum-Deposited Perovskite Solar Cells. *Chemistry of Materials* **2019**, *31*, 6945-6949.

9. Zhao, Y.; Nardes, A. M.; Zhu, K., Effective Hole Extraction Using MoO_x-Al Contact in Perovskite $CH_3nNH_3PbI_3$ Solar Cells. *Applied Physics Letters* **2014**, *104*, 213906.

10. Wang, Q.-K.; Wang, R.-B.; Shen, P.-F.; Li, C.; Li, Y.-Q.; Liu, L.-J.; Duhm, S.; Tang, J.-X., Energy Level Offsets at Lead Halide Perovskite/Organic Hybrid Interfaces and Their Impacts on Charge Separation. *Advanced Materials Interfaces* **2015**, *2*, 1400528.

11. Liu, P.; Liu, X.; Lyu, L.; Xie, H.; Zhang, H.; Niu D.; Huang, H.; Xiao, .; Huang, J.; Gao, Y., Interfacial Electronic Structure at the $CH_3NH_3PbI_3/MoO_x$ Interface. *Applied Physics Letters* **2015**, *106*, 193903.

12. Li, L.; Wand, C.; Wang C.;Tong, S.; Zhao, Y.; Xia, H.; Shi J.; Shen, J.; Xie, H.; Liu, X.; Niu, D.; Yang, J.; Huang, H.; Xiao, S.; He, J.; Gao, Y., Interfacial Electronic Structures of MoO_x/Mixed Perovskite Photodetector. *Organic Electronics* **2019**, *65*, 162-169.

13. Thibau, E. S.; Llanos, A.; Lu, Z.-H., Disruptive and Reactive Interface Formation of Molybdenum Trioxide on Organometal Trihalide Perovskite. *Applied Physics Letters* **2017**, *110*, 081604.

14. Li, L.; Liu, X.; Lyu, L.; W, R.; Liu, P.; Zhang, Y.; Zhao, Y.; Huang, H.; Niu, D.; Yang, J.; Gao, Y., Modification of Ultrathin Npb Interlayer on the Electronic Structures of the $CH_3NH_3PbI_3$/NPB/MoO_3 Interface. *The Journal of Physical Chemistry C* **2016**, *120*, 17863-17871.

15. Lee, M. M.; Teuscher, J.; Miyasaka, T.; Murakami, T. N.; Snaith, H. J., Efficient Hybrid Solar Cells Based on Meso-Superstructured Organometal Halide Perovskites. *Science* **2012**, *338*, 643-647.

16. Liao, X.; Jeong, A. R.; Wilks, R. G.; Wiesner, S.; Rusu, M.; Bär, M., X-Ray Irradiation Induced Effects on the Chemical and Electronic Properties of MoO_3 Thin Films. *Journal of Electron Spectroscopy and Related Phenomena* **2016**, *212*, 50-55.

17. Liao, X.; Jeong, A. R.; Wilks, R. G.; Wiesner, S.; Rusu, M.; Félix, R.; Xiao, T.; Hartmann, C.; Bär, M., Tunability of MoO_3 Thin-Film Properties Due to Annealing in Situ Monitored by Hard X-Ray Photoemission. *ACS Omega* **2019**, *4*, 10985-10990.

18. Gorgoi, M.; Svensson, S.; Schäfers, F.; Öhrwall,G.; Mertin, M.; Bressler, P.; Karis O.; Sigbahn,H.; Sandell, A.; Rensmo, H.; Doherty, W.; Jung, C.; Braun, W.; Eberhardt, W., The High Kinetic Energy Photoelectron Spectroscopy Facility at Bessy Progress and First Results. *Nuclear Instruments and Methods in Physics Research Section A: Accelerators, Spectrometers, Detectors and Associated Equipment* **2009**, *601*, 48-53.

19. Schaefers, F.; Mertin, M.; Gorgoi, M., Kmc-1: A High Resolution and High Flux Soft X-Ray Beamline at Bessy. *Rev. Sci. Instrum.* **2007**, *78*, 123102.

20. Shinotsuka, H.; Tanuma, S.; Powell, C. J.; Penn, D. R., Calculations of Electron Inelastic Mean Free Paths. X. Data for 41 Elemental Solids over the 50 eVv to 200 KeV Range with the Relativistic Full Penn Algorithm. *Surf. Interface Anal.* **2015**, *47*, 871-888.

21. Tanuma, S.; Powell, C. J.; Penn, D. R., Calculations of Electron Inelastic Mean Free Paths. V. Data for 14 Organic Compounds over the 50–2000 eV Range. *Surf. Interface Anal.* **1994**, *21*, 165-176.

22. Wang, C.; Irfan, I.; Liu, X.; Gao, Y., Role of Molybdenum Oxide for Organic Electronics: Surface Analytical Studies. *Journal of Vacuum Science & Technology B, Nanotechnology and Microelectronics: Materials, Processing, Measurement, and Phenomena* **2014**, *32*, 040801.

23. Hartmann, C.; Sadoughi, G.; Félix, R.; Handick, E.; Klemm, H. W.; Peschel, G.; Madej, E.; Fuhrich, A. B.; Liao X.; Raoux, S.; Abou-Ras, D.; Wargulski, D.; Schmidt, T.; Wilks. R. G.; Snaith, D.; Bär,M., Spatially Resolved Insight into the Chemical and Electronic Structure of Solution-Processed Perovskites—Why to (Not) Worry About Pinholes. *Advanced Materials Interfaces* **2018**, *5*, 1701420.

24. Philippe, B.; Park, B.-W.; Lindblad, R.; Oscarsson, J.; Ahmadi, S.; Johansson, E. M. J.; Rensmo, H., Chemical and Electronic Structure Characterization of Lead Halide Perovskites and Stability Behavior under Different Exposures—a Photoelectron Spectroscopy Investigation. *Chemistry of Materials* **2015**, *27*, 1720-1731.

25. Matteocci, F.; Busby, Y.; Pireaux, J.-J.; Divitini, G.; Cacovich, S.; Ducati, C.; Di Carlo, A., Interface and Composition Analysis on Perovskite Solar Cells. *ACS Applied Materials & Interfaces* **2015**, *7*, 26176-26183.

26. Eames, C.; Frost, J. M.; Barnes, P. R. F.; O'Regan, B. C.; Walsh, A.; Islam, M. S., Ionic Transport in Hybrid Lead Iodide Perovskite Solar Cells. *Nature Communications* **2015**, *6*, 7497.

27. Sadoughi, G.; Starr, D. E.; Handick, E.; Stranks, S. D.; Gorgoi, M.; Wilks, R. G.; Bär, M.; Snaith, H. J., Observation and Mediation of the Presence of Metallic Lead in Organic–Inorganic Perovskite Films. *ACS Applied Materials & Interfaces* **2015**, *7*, 13440-13444.

28. Moore, D. T.; Sai, H.; Tan, K. W.; Smilgies, D.-M.; Zhang, W.; Snaith, H. J.; Wiesner, U.; Estroff, L. A., Crystallization Kinetics of Organic–Inorganic Trihalide Perovskites and the Role of the Lead Anion in Crystal Growth. *Journal of the American Chemical Society* **2015**, *137*, 2350-2358.

29. Juarez-Perez, E. J.; Ono, L. K.; Maeda, M.; Jiang, Y.; Hawash, Z.; Qi, Y., Photodecomposition and Thermal Decomposition in Methylammonium Halide Lead Perovskites and Inferred Design Principles to Increase Photovoltaic Device Stability. *Journal of Materials Chemistry A* **2018**, *6*, 9604-9612.

30. Juarez-Perez, E. J.; Hawash, Z.; Raga, S. R.; Ono, L. K.; Qi, Y., Thermal Degradation of $CH_3NH_3PbI_3$ Perovskite into NH_3 and CH_3I Gases Observed by Coupled Thermogravimetry–Mass Spectrometry Analysis. *Energy Environ. Sci.* **2016**, *9*, 3406-3410.

31. Godding, J. S. W.; Ramadan, A. J.; Lin, Y.-H.; Schutt, K.; Snaith, H. J.; Wenger, B., Oxidative Passivation of Metal Halide Perovskites. *Joule* **2019**, *3*, 2716-2731.

32. Jain, S. M.; Philippe, B.; Johansson, E. M. J.; Park, B.-w.; Rensmo, H.; Edvinsson, T.; Boschloo, G., Vapor Phase Conversion of PbI_2 to $CH_3NH_3PbI_3$: Spectroscopic Evidence for Formation of an Intermediate Phase. *Journal of Materials Chemistry A* **2016**, *4*, 2630-2642.

33. Quarti, C.; Grancini, G.; Mosconi, E.; Bruno, P.; Ball, J. M.; Lee, M. M.; Snaith, H. J.; Petrozza, A.; De Angelis, F., The Raman Spectrum of the $CH_3NH_3PbI_3$ Hybrid Perovskite: Interplay of Theory and Experiment. *The Journal of Physical Chemistry Letters* **2014**, *5*, 279-284.

34. Park, B.-W.; Jain, S. M.; Zhang, X.; Hagfeldt, A.; Boschloo, G.; Edvinsson, T., Resonance Raman and Excitation Energy Dependent Charge Transfer Mechanism in Halide-Substituted Hybrid Perovskite Solar Cells. *ACS Nano* **2015**, *9*, 2088-2101.

35. Le, F. R.; Oh, W.; Reece, I.; Werner, R., Infra-Red Absorption Spectra of Metal Hyponitrites. *Australian Journal of Chemistry* **1957**, *10*, 361-364.

36. Zabinski, J. S.; Day, A. E.; Donley, M. S.; Dellacorte, C.; McDevitt, N. T., Synthesis and Characterization of a High-Temperature Oxide Lubricant. *Journal of Materials Science* **1994**, *29*, 5875-5879.

37. Merlen, A.; Buijnsters, J. G.; Pardanaud, C., A Guide to and Review of the Use of Multiwavelength Raman Spectroscopy for Characterizing Defective Aromatic Carbon Solids: From Graphene to Amorphous Carbons. *Coatings* **2017**, *7*, 153.

38. Azarang, M.; Aliahmad, M.; Shiravizadeh, A. G.; Azimi, H. R.; Yousefi, R., Zn-Doped PbO Nanoparticles (NPs)/Fluorine-Doped Tin Oxide (FTO) as Photoanode for Enhancement of Visible-near-Infrared (NIR) Broad Spectral Photocurrent Application of Narrow Bandgap Nanostructures: SnSe NPs as a Case Study. *Journal of Applied Physics* **2018**, *124*, 123101.

39. Yousefi, R.; Jamali-Sheini, F.; Cheraghizade, M.; SA'Aedi, A., Facile Synthesis and Optical Properties of PbO Nanostructures. *Latin American Applied Research* **2014**, *44*, 159-162.

40. Zhao, R.; Zhang, K.; Zhu, J.; Xiao, S.; Xiong, W.; Wang, J.; Liu, T.; Xing, G.; Wang, K.; Yang, S.; Wang X., Surface passivation of organometal halide perovskites by atomic layer deposition: an investigation of the mechanism of efficient inverted planar solar cells. *Nanoscale Adv.* **2021**, DOI: 10.1039/D1NA00075F. (in press)

Table of Contents graphic